Analyst

RSC Publishing

PAPER

View Article Online
View Journal | View Issue

Cite this: *Analyst*, 2013, **138**, 5371

In vivo characterization of protein uptake by yeast cell envelope: single cell AFM imaging and μ-tip-enhanced Raman scattering study†

Denys Naumenko,[a] Valentinas Snitka,[a] Elena Serviene,[bc] Ingrida Bruzaite[b] and Boris Snopok*[a]

Direct detection of biological transformations of single living cells *in vivo* has been performed by the advanced combination of local topographic imaging by Atomic Force Microscopy (AFM) and label-free sub-surface chemical characterization using new μ-Tip-Enhanced Raman Spectroscopy (μ-TERS). The enhancing mechanism for μ-TERS tips with micrometre range radius differs significantly to that of the conventional tapered structures terminated by a sharp apex and conditioned by the effects of propagating instead of localizing surface plasmon resonance phenomena. Sub-wavelength light confinement in the form of a nonradiative evanescent wave near the tip surface with penetration depth in the sub-micrometre range opens the way for monitoring of subsurface processes near or within the cell wall, inaccessible by other methods. The efficiency of the approach has been demonstrated by the analysis of the cell envelope of genetically modified (by glucose dehydrogenase (GDH) gene bearing *Kluyveromyces lactis* toxin signal sequence) yeast cells enriched by GDH protein. The presence of transmembrane fragments in GDH together with the tendency to form active dimers and tetramers causes the accumulation of the proteins within the periplasmic space. These results demonstrate that the advanced combination of AFM imaging and subsurface chemical characterization by the novel μ-TERS technique provides a new analytical tool for the investigation of single living cells *in vivo*.

Received 20th February 2013
Accepted 24th June 2013

DOI: 10.1039/c3an00362k

www.rsc.org/analyst

Introduction

Micro- and nano-local optical characterization of animate nature (*e.g.* cells, tissues, animalcular organisms *etc.*) can be efficiently used to see the details of living matter *in vivo*.[1,2] The most important advantage of the optical technique is the ability to perform longitudinal studies of living beings to identify and characterize biological processes in their unperturbed natural conditions. Indeed, the on-line monitoring of the biochemical status of single living cells represents the ultimate limit in cell biology; one can obtain insight into a biochemical status of an individual cell and monitor its changes without resorting to ensemble averages.

Classical bio-optical approaches based on infrared absorption, various Raman scattering and fluorescence techniques *etc.* are of fundamental importance in exploring the physical and chemical properties of biological samples for functional visualization.[3,4] However, in order to resolve the design of the functional cellular substructures, *in situ* optical fields have to be confined to the same scale in order to obtain sufficiently high 1D, 2D or 3D resolution to perform the corresponding local subsurface, surface or spatial chemical characterization.[5]

A major challenge for identification and local chemical characterization of subcellular components is how to deliver and concentrate light from the micron-scale into the nano-scale in a given area of space. Light cannot be guided, by conventional mechanisms, with optical beam sizes significantly smaller than its wavelength due to the diffraction limit. To some extent, this problem was solved by developing the Scanning Near-field Optical Microscopy (SNOM) where a Scanning Probe Microscope (SPM) serves as a suitable tool for spatial nano-positioning and confinement of a light source to an aperture realizing the near-field optical readout. However both SPM and SNOM generally lack the ability to perform label-free chemical characterization of the materials.[6]

A practical implementation of local aperture-less optical spectroscopy with ultrahigh spatial resolution, so-called Tip-Enhanced Raman Spectroscopy (TERS), has become possible by combining vibrating optical spectroscopy and scanning probe microscopy.[7–10] This possibility of local targeting of the Raman scattering effect is pushing optical spectroscopy to the nano-scale. To obtain ultimate lateral optical resolution, TERS uses

[a]*The Research Centre for Microsystems and Nanotechnology, Kaunas University of Technology, Studentu 65, 51369, Kaunas, Lithuania. E-mail: vsnitka@ktu.lt; b_snopok@yahoo.com; Fax: +370 37 451588; Tel: +370 37 451588*

[b]*Vilnius Gediminas Technical University, Department of Chemistry and Bioengineering, Sauletekio al. 11, 10223, Vilnius, Lithuania*

[c]*Nature Research Centre, Akademijos 2, 08412, Vilnius, Lithuania*

† Electronic supplementary information (ESI) available. See DOI: 10.1039/c3an00362k

strongly localized field enhancement, where this enhanced interaction volume acts as an excitation source. This is particularly critical for the Raman effect that, as an inelastic scattering process, is weak, so the concentration of the optical energy and additional scattering enhancement is necessary for sensitive enough optical readout.

An enhancement of Raman signals can be implemented by magnification of the incident electromagnetic field, amplification of Raman scattering emission and direct modification of the scattering process itself, producing an effectively larger cross-section than would occur from the molecule alone ("chemical"[11,12] enhancement or "gradient-field Raman"[13,14] effect). The first two mechanisms usually refer to electromagnetic origin: for a molecule nearby on the nano-sized "antenna", its Raman scattering field is enhanced in the same way as is the incident laser field.[15] Therefore, the incident and scattered fields increase by about the same amount, and the Raman signal scales roughly with the fourth power of the local optical field enhancement.[11] Enhancement is particularly strong when both incident and scattered fields are in resonance with the electromagnetic excitations in "antenna".[16] However, if the distance from an "antenna" is increasing, the resonance conditions have been broken, and processes of Raman scattering enhancement become additive rather than resonance.

The large enhancement of local electromagnetic fields can be realized on the surface of Drude metals (*e.g.* gold, silver, *etc.*). Spatial confinement of light can be implemented by (i) generation of propagating surface plasmon resonance (surface localization),[17,18] (ii) excitation of localized surface plasmon resonance (localization near the nanostructure),[19,20] (iii) as the result of the constructive interference *etc.* of the fields from (i) and (ii) ("hot spots") as well as (iv) the result of pure geometric phenomena related to field lines crowding near sharp tips, narrow gaps *etc.* ("lighting rod effect"[21]). For the metal SPM tip, a typical way to concentrate optical energy and enhance the electric field around it is to confine light in the form of an evanescent wave using a plasmonic taper.[22]

A surface plasmon polariton (SPP) is an electromagnetic excitation (surface wave) existing on the surface of Drude materials.[18,23] It is an intrinsically two-dimensional excitation whose electromagnetic field decays exponentially with distance from the surface. SPPs can propagate, scatter, interfere, and localize *etc.* depending on both local (nanometre scale[24]) as well as macro (micrometer scale[25]) characteristics of the surface profile.[26,27] Focusing of light into very small volumes beyond the diffraction limit can be achieved by exploiting the wavelength scalability of surface plasmon polaritons.[28,29] One of the simplest ways to achieve focusing of SPP is based on using tapered metallic structures (*e.g.* tapered metal rods *etc.*) guiding SPP modes; by slowing down an optical wave and shrinking its wavelength during its propagation, optical energy can be compressed and concentrated down to the nanometre scale.[29–31] Besides the classical TERS with sharp tips, focusing of SPPs by a spherical or otherwise curved metal surface whose sizes are approximately that of the light wavelength are attractive for the design of sensing probes with 1D subsurface nanoscale resolution in the direction along the tip axis. This structure is shown to combine the benefits of focusing due to SPP annular propagation towards the tip of the hemisphere[25,32] *etc.* and potential of propagating surface plasmon resonance effects.[18,33,34] Moreover, the mass production of reproducible μ-TERS tips can be easily realized by using the equipment of classical microelectronic technologies that open the way to overcoming the bottleneck in the wide application of the technology.

The focusing mechanism for μ-TERS tips with micrometer range radius differs significantly to the conventional tapered structures terminated by a sharp tip.[28–31,35,36] Indeed, due to the large radius of curvature of the probe termination (up to μm range), the SPP may propagate continuously along the tip surface and then back in the opposite direction with relatively low radiation loss. This is in contrast to the classical nanofocusing tapered structures where the very small radius of curvature at the tip (~5 to 20 nm) results in significant accumulation of optical energy at the tip: the SPPs are slowed down and adiabatically stopped at the apex depositing a significant fraction of their energy to the tip. Contrary to that, the SPP propagation along the curved metal surface with diameters approximately that of the light wavelength or larger, seem similar to the situation at the flat metal surface. In this case the electromagnetic energy is compressed in the area occupied by the nonradiative evanescent wave in dielectric that can be modulated by the interference at the tip apex.[25] It is reasonable to note that physical mechanisms of light localization are similar for both inhomogeneous plane Zenneck waves and axial symmetrical Sommerfeld–Goubau waves at the flat and cylindrical metal surfaces respectively.[37]

The local field enhancement can be significantly reduced by radiative losses. The radiation effect of the SPP focusing is dependent on the radius of curvature; the SPP is nonradiative at the "ideal flat" (roughness less) surface,[18] SPP propagation around bends at metal–dielectric interfaces can generate some additional curvature induced radiation,[25,38,39] whereas significant radiative loss is observed only at corners *etc.*[35,36] For example, typical radiation losses of SPPs owing to surface roughness (root mean square value above 1 nm) of the thin polycrystalline gold films are greater than 2–3% of the incident beam.[40,41]

Both the spatial resolution and enhancement factor of TERS have been determined by the region at the apex of the tip. The enhancement factor of the Raman scattering from an object near the sharp tip (usually with radius less than 20 nm) is often 10^7, or more.[42] Some of the best resolutions reported were obtained for carbon nanotubes (~10 nm with tips of 10–15 nm radius)[43,44] and laser dyes (~15 nm with a 20 nm radius tip)[45,46] *etc.* which have high Raman scattering cross-sections. The penetration depth of the electromagnetic field into the medium below the sharp tip apex of 10–20 nm radius is less than a few tens of nanometers,[10,47,48] so subsurface imaging is impossible. However, with the increase of the tip radius the region of space occupied by the evanescent wave is extended up to the order of the wavelength on a flat surface.[18,49,50] And whilst the intensity of the electromagnetic field, the resolution and the field enhancement at the tip apex is reduced, it nevertheless provides the possibility to extend the TERS approach to a new class of biological problems.

Despite the significant benefits of the classic high-resolution TERS methods, the solution of many biological problems requires a much smaller spatial resolution in some directions due to the peculiarities inherent to living things *qua* living things. As an example we refer to the fast degradation of biological membranes under illumination[51] resulting in the requirement to use only small-intensity laser beams for the analysis of single living cells. With regards to the quite low cross-section of the Raman processes, the signal that can be detected by standard diffraction-limited optics in the far field is relatively weak; so, long acquisition times are required. As most of the membrane structures are not fixed and move on the surface of cells—a typical speed for a membrane phospholipid is 2 μm per second[52]—local chemical analysis of living cells is ambiguous in many cases. An additional factor is the natural vibration of the cell membrane, which determines the feasibility of statistically correct spatial averaging of space-dependent processes or cells' mechanical fixation. Moreover, features of the spatial modulation of the SPM probe can also give rise to certain spatial ambiguity. For example, the displacement of the tip glued to the piezoelectric tuning fork actuators (as probes in shear force SPM mode) may reach the sub-micrometer range during vibrations.[53] The latter effect also determines the need for spatial averaging within the measurement area to obtain a statistically correct result. μ-TERS technology with relatively low lateral resolution determined by the tip geometry provides this averaging in a natural way. In other words, contrary to the high-resolution TERS with maximum scope restricted roughly[54] by $R \times R \times R$ (R is the tip radius in nanometer range), in the μ-TERS we can highlight the volume with $R \times R \times \lambda$ in size (λ is the light wavelength, R in sub-micrometer range). So, instead of the ultimate 3D resolution we obtain the techniques for the 1D analysis of buried nanoscale features with the possibility to control the penetration depth of the evanescent wave inside the object volume by the changing the tip–surface distance d.

The characterization of subsurface features poses a challenge for the monitoring of membrane related process, especially in the case of the relatively thick cell walls with a thickness greater than 100 nm (yeasts, plant cells *etc.*). The ability to access and characterize buried molecular structures holds great promise in applications such as the detection of protein–membrane interactions, protein localization or membrane related transport.

In the present work we discuss the biochemical and topographical changes in the yeast cell envelope induced by genetic modification. To perform the nanoscale topographical analysis of single living cells we used Atomic Force Microscopy (AFM) imaging, whereas the cell envelope specific chemical analysis is performed by μ-tip-enhanced Raman scattering spectroscopy (μ-TERS). The utility of the approach is exemplified by the detection of glucose dehydrogenase (GDH) protein accumulation in the cell envelope of genetically modified *Saccharomyces cerevisiae* yeast cells, one of the most extensively studied model eukaryotic organisms.

The paper is organized as follows: it begins by discussing the methodological aspects of the μ-TERS spectroscopy measurements, a cell modification protocol, experimental setups, tip preparation *etc.* This is followed by a detailed analysis of our experimental data and peculiarities of the cell biochemistry and morphology induced by genetic modification obtained by AFM imaging, conventional confocal μ-Raman and μ-TERS spectroscopies. Finally, the mechanism of GDH accumulation by the cell envelope is discussed.

Materials and methods

Yeast cell modification

The yeast secretion plasmid pYEsec1-GDH (Fig. 1), bearing *Acinetobacter calcoaceticus* glucose dehydrogenase gene (GenBank accession number GC657400.1) was obtained by the insertion of a *GDH* sequence into the pYEsec1 plasmid[55] downstream of the GAL-CYC1 promoter and in frame with *Kluyveromyces lactis* toxin signal sequence (for secretion of the GDH into extracellular media). For this purpose, GDH was PCR-amplified from bacterial plasmid pAI3-PT15 (Patent no. WO2004099399) by forward primer GDH sec_{Fw} 5′-GCATGGATCCAATAAACATTTATTGGC-3′ and reverse primer GDH ab_{Rw} 5′-AACACGGTCTCAGCGCTCTGAGCTTTATATG-3′, cut by *BamHI* and *PstI* restriction enzymes and ligated to the receiving vector pYEsec1.[56]

General procedures for the construction and analysis of recombinant DNAs were performed according to ref. 57. Restriction enzymes (*Bam*HI, *Pst*I), T4 DNA ligase, bacterial alkaline phosphatase, Pfu DNA polymerase and DNA size marker (GeneRuler™ DNA Ladder mix) were purchased from Fermentas (Vilnius, Lithuania) and used following the manufacturer's recommendations.

The *E. coli* strain DH5α (F^- (ϕ80dΔ(lacZ)M15) recA1 endA1 gyrA96 thi1 hsdR17 ($r_k^- m_k^+$) supE44 relA1 deoR Δ(lacZYA-argF)-U169)[58] was used in cloning experiments, plasmid isolation and maintenance. The transformation of *E. coli* was carried out using calcium chloride method or electroporation.[59]

Plasmid DNAs were isolated by the alkaline lysis method[60] and column-purified according to manufacturer's recommendations (Fermentas, Vilnius, Lithuania).

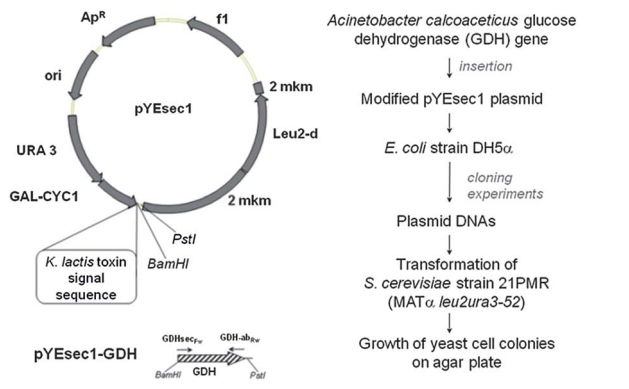

Fig. 1 Principal scheme of pYEsec1-GDH plasmid (left) and sample preparation (right). *URA*3, *Leu*2-d – genetic markers; 2mkm – sequence originated from 2 μ plasmid of *S. cerevisiae*; ApR – gene for β-lactamase; ori – pMB1 replication origin; GAL-CYC1 – galactose inducible promoter; f1 – f1 bacteriophage replication origin; *GDH* – glucose dehydrogenase gene; Fw and Rw – marked forward and reverse primers; *BamHI*, *PstI* – restriction endonuclease sites.

For the expression of *GDH* construct, *S. cerevisiae* strain 21PMR (MATα*leu2ura3-52*) was used (kindly provided by Dr T. Jokantaite). The transformation of *Saccharomyces cerevisiae* strains was performed following the LiAc/PEG method[61] and the transformants were selected by complementation of *URA3* auxotrophy. The media for propagation of *S. cerevisiae* yeast, as well as standard genetic techniques have been described in ref. 59.

For the purpose of GDH protein purification, the yeast cells were harvested by centrifugation (3000 *g*) at 4 °C for 10 min; the resultant biomass (1 g) was re-suspended in 2 ml of A buffer (50 mM Tris–HCl, pH 8.5) and ground using liquid nitrogen. The cell extract (cytoplasmic fraction) was cleared by centrifugation (11 000 *g*) at 4 °C for 15 min. The sediments (membrane fraction) were dissolved by suspending and incubating them in A buffer with 1% Triton X-100 at 4 °C for 1 h. The protein purification was performed by ion-exchange chromatography on a CM-cellulose column according to the manufacturer's instruction (GE Healthcare) and dialysis against PBS buffer. The concentration and purity of proteins were estimated by densitometric analysis of samples run on 15% SDS-PAGE; the gels were visualized using Coomassie Brilliant Blue. The specific activity of GDH (U ml^{-1}) was determined in a crude yeast extract and in cytoplasmic or membrane fractions by measuring the decrease in DCIP absorbance at 600 nm.

Sample preparation

The wild type (21PMR) and genetically modified (21PMR-[pYE-sec1-GDH]) *S. cerevisiae* yeast strains were grown onto YPG agar (1% yeast extract, 2% peptone, 3% galactose, 2% agar) plates for 24 h at 30 °C. For the preparation of samples for AFM and Raman spectroscopic measurements, the agar-grown cells were transferred onto sterilized 50 × 24 × 0.17 mm^3 (Carl Roth, Germany) cover slips and kept in a Petri dish for 1–2 hours prior to imaging. We did not use any coating on the slide glass to immobilize the cells nor any additional mechanical or chemical fixation. For the transfer of the cells the cover slip was placed on the colony's upper side and carefully removed with usually monolayers of the cells on the glass. This procedure preserves the natural conditions for yeast cell growth since *S. cerevisiae* yeast reproduce, as a rule, on the surface of solid or liquid media. It is well known that a yeast population demonstrates the ability of thermoresistance in the range from 12 °C up to 40 °C.[62,63] This is due to the adaptive activity of the cells' chemosmotic system which allows for maintaining a high reproduction rate in yeast when the ambient temperature is changing over a relatively wide temperature range. In line with that, all experiments were performed at room temperature (20 ± 2 °C) without additional thermo stabilization.

Atomic force microscopy measurements

Cells were characterized by AFM (NTEGRA Spectra system, NT-MDT Inc., Russia) in an 'upright' configuration in the tapping mode using commercial silicon cantilevers NSG11 with a force constant of 5 N m^{-1} (for topography images) at a scan rate of typically 1 Hz or in the contact mode using CSG10 cantilevers with a force constant of 0.1 N m^{-1} (for characterization of membrane elastic properties).

μ-Tip enhanced Raman spectroscopy

Two frequently used techniques for the fabrication of metallic tips are electrochemical etching and metal evaporation on AFM tips.[23,31,54,64] In the electrochemical etching method, a voltage is applied between a wire and a second metallic electrode, both immersed in concentrated hydrochloric acid solution.[65,66] In the present work the tips as well were produced by the electrochemical etching (10 V, 10 kHz, 10–30 s) of thin gold wire in a $CaCl_2$ saturated solution twice diluted with water.[67] Before etching, the gold wire was cleaned and glued to a quartz tuning fork transducer. For etching, a 99.99% pure gold wire of 125 μm diameter was used (GoodFellow, Cambridge Limited, England). The fabricated tuning fork based probes have an apex diameter in the sub-micrometer range (typically 400–600 nm) and show a *Q*-factor value greater than 500–700 at a resonant frequency of above 190 kHz.

A typical image of the produced tips is presented in Fig. 2. As the figure shows, the metal tip, obtained by one-step electrochemical etching, is a cone of bulk metal with a rough surface. Coupling between external radiation and plasmon states at the tip surface is possible through diffraction of the external radiation on the rough surfaces ("1", Fig. 2).[68] Under the bottom illumination using the 100× objective with a numerical aperture of 1.32, immersion oil (Immersol 518F, Carl Zeiss, Germany) and a glass slide with a refractive index of 1.51, the incident angles for the light illuminating the tip (with the apex angle *e.g.* 45°) will be in the range from 0° to greater than 110° in respect to the tip surface. Under those conditions the excitation of SPP at the rough surface of gold is quite usual. In recent years, surface gratings (created by microlithography) have become available and studies of surface plasmon excitation using these gratings have become most useful.[69]

Surface waves propagate in various directions reflecting on steric hindrance, interact and decay ("2" and "3", Fig. 2) by spreading along a rough surface. The intensity of the surface state may be caused by single or multiple scatterings. The last process includes repetitive nonradiative elastic scattering of plasmon waves at a rough surface with changes in propagation direction without loss of energy ("5", Fig. 2). We have here a good example of strong in-plane reflection and interference of surface waves on the stochastic relief.[40] This leads to a decrease of wave propagation in media, the formation of localized states ("hot spots") of the surface wave, and it is followed by radiative decay and irradiation of the electromagnetic waves into the surroundings. Thus, elastic repetitive nonradiative scattering on the tip surface (uniformly on the tip surface, not only at the tip apex) and consequent single radiative scattering may be a principal radiative loss mechanism of surface electromagnetic excitations. For the tips under consideration with relatively low curvature the intensity of radiative scattering is small and similar to one at the flat surface; its intensity and scattering directions are determined by the power of spectral density of the tip surface profile (roughness).[40]

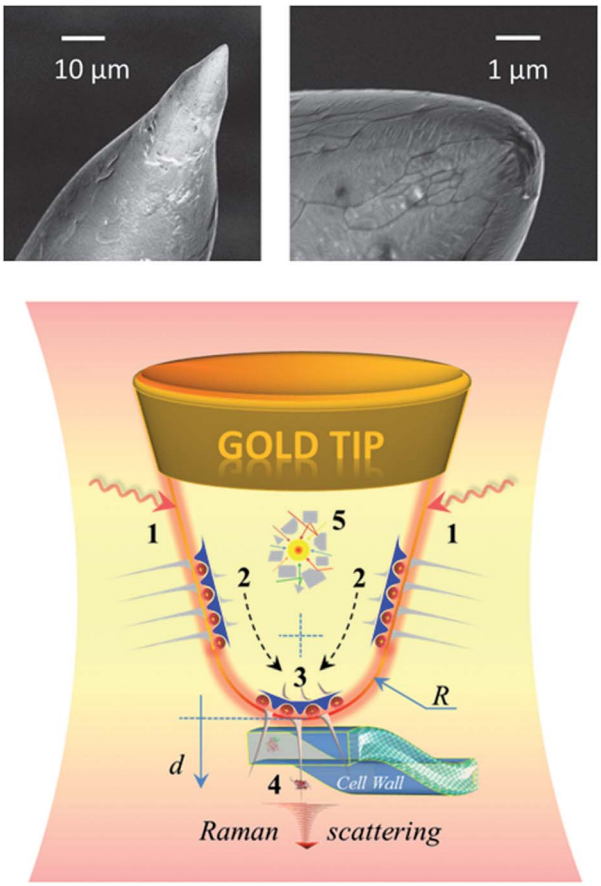

Fig. 2 The top pictures are scanning electron microscope images of the μ-TERS tip. The schematic diagram of the core processes (bottom) is illustrating the generation and propagation of surface plasmon polaritons at the surface of the tip in the focal plane of the microscope in the case of large tip radius *R*. Coupling between external radiation and plasmon states is possible through diffraction of the external radiation on the rough surface of the tip (process "1"). SPP excitations propagate along the tip axis (process "2", indicating also the penetration depth of evanescent waves) due to the geometry of the tip and possibly interfere at the apex (process "3"); increased electromagnetic field near the tip polarizes the electron shells of molecules in the area occupied by the evanescent wave (process "4") and enhance Raman scattering. Process "5" illustrates the formation of radiated "hot spots" on the surface of the tip due to the interference on the stochastic surface relief.

Due to the tip geometry, surface waves tend to spread to the apex (by multiple changes in propagation directions without essential loss of energy), causing thus an additional concentration field due to the possible constructive interference ("3", Fig. 2). It should also take into account the changes in the spatial distribution of the evanescent wave for the different diameters of the probe.[70] The energy flow of the electromagnetic states is confined mainly in the dielectric with the maximum intensity of the electric field at the surface of the metal ("4", Fig. 2). With the increase of the diameter of the probe, the interfacial process is more and more similar to that on the flat surface of the metal.[18] Regardless of the radius of the tip, exponential decay of the field in the surface region is preserved, and the intensity of the electric field below the tip apex decays exponentially as $\exp(-d/R)$, where d is the distance from the tip apex and R the tip radius.[71] Whilst such a description is not strictly accurate as R tends to infinity, it provides clear qualitative insight. When $R = 20$ nm, the intensity of the electric field at a distance $d = 100$ nm from the tip is less than 1% of that on the metal surface; the excitation is high localized in the area immediately adjacent to the tip. However, at $R = 200$ nm, this value is about 60%; more than enough to polarize and excite the electronic states of the molecules at a distance of 100 nm from the tip apex.

Use dependency probably overestimates the value of the field at a large tip radii, but qualitatively correctly describes the actual situation according to various experimental studies.[71] In particular, polycrystalline gold films with a crystallite size in the range of 30–50 nm demonstrate very low radiation losses[40,41] which suggests that the spatial heterogeneities of this size do not prevent the spread of SPP and do not cause essential radiation losses. If neglecting possible additional enhancement of the field due to the constructive interference and focusing of surface waves directed toward the tip, the best lower estimate for the penetration depth of the evanescent wave is one for a flat surface. In line with ref. 18, for the classic version of SPP in thin gold films, the penetration depth δ of an evanescent wave (decays exponentially as $\exp(-d/\delta)$) into a medium with a lower refractive index is about 37% of the wavelength λ.[18] So, for that used in this work, $\lambda = 632.8$ nm, the penetration depth δ will be greater than 233 nm. It should be stressed that the intensity of the evanescent wave decreases with increasing distance from the surface, so the effective area of intersection of the same object with the field at different distances from the surface also changes.[18] This leads to a nonlinear influence of the field on the molecular components of the sample located at different distances from it. However, the localized optical field itself is still significant enough at a distance of 100–200 nm from the tip and extends into the space up to the order of the wavelength.

Raman spectroscopy measurements

Raman spectra of individual cells are measured using a confocal Raman system (NTEGRA Spectra, NT-MDT, Russia) that has been described previously.[72] In case of 'inverted' configuration (Fig. 3, 'I') a 35 mW He–Ne laser (632.8 nm, Melles Griot 25-LHP-928-230, USA) or a 20 mW DPSS laser (532 nm, LCM-S-111-20-NP25, Russia) were used. The laser beam is delivered through a clean-up filter into an inverted optical microscope (Nikon Eclipse TE 2000-S). The microscope is equipped with a 100× 1.32 numerical aperture oil immersion objective (Leitz NPL Fluotar, Germany), resulting in diameter of the spot less than 0.3 μm at the laser focus. In the present work we used partly unfocused laser beam with above 5 μm in diameter that entire cover the single yeast cell. Typical laser powers at the focus can be controlled in the range of 0.01–10 mW. The beam is focused through a glass cover slip of thickness 0.15 mm (Carl Roth, Germany), which rests on a controlled *XY* stage capable of scanning samples over a 50 × 50 μm. The cells on the cover slips are probed by the laser beam and scattered signals are collected for the same objective and then focused through a 100 μm pinhole. A 633 or 532 nm ultrasteep long-pass edge filters reject

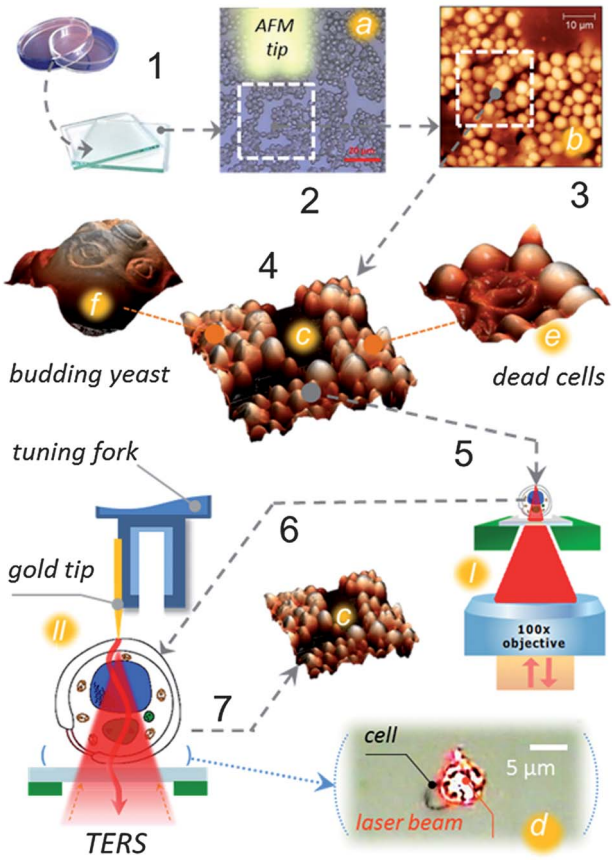

Fig. 3 Schematic diagram of core procedures is illustrating the analysis of yeast cells: (1) sample preparation; (2) general optical imaging; (3) topographic characterization by AFM imaging; (4) cell selection; (5) single cell μ-Raman investigations; (6) μ-TERS measurements; (7) verifying AFM analysis of cells integrity. (I) 'inverted' and (II) μ-TERS experimental configuration, based on tuning-fork shear-force AFM tip. 'a' – typical optical image of cells colonies, 'b', 'c', 'e', and 'f' – typical AFM images of the samples, 'd' – optical image illustrating the size of the yeast cell and laser beam on the glass slide.

residual backscattered laser light and the signal is directed into a spectrometer (Solar TII, NT-MDT) equipped with a TE-cooled (−60 °C) CCD camera (DV401-BV, Andor Technology, USA). The additional CCD camera is used to collect microscope images of the cells being probed.

The μ-tip-enhanced Raman measurements (Fig. 3, 'II') were performed on the same inverted configuration (Fig. 3, 'I'). Using the additional Scanning Probe Microscopy platform (for shear-force mode with tuning fork piezoelectric linear actuator, average displacement under oscillations is less than 50 nm), the apex of the gold tip was positioned to the focused beam on the measured sample. Finally, a conventional Raman microscopy set-up was coupled with a SPM for synchronized use (TERS mode of the NTEGRA Spectra system).

Spectral preprocessing

Raman spectra were collected within the spectral region from 1200 to 1700 cm^{-1}. This region is known as the molecular fingerprint region and provides the most information on the biological constituents of yeast cells. Following the spectral acquisition, the background spectrum originating from the cover glass and other optical elements was first subtracted from each cell spectrum. The spectra than have been averaged for 10 raw records and the final spectrum were corrected from the fluorescence input by subtraction of a third-order polynomial curves using Raman Processing Program.[73,74]

The band specific experimental Raman enhancement factor G_s has initially been deduced from the increase in intensity within the specific Raman bands using

$$G_s = \int_{\delta_n-\Delta}^{\delta_n+\Delta} I(\delta)\mathrm{d}\delta \quad (1)$$

where $I(\delta)$ is the intensity of averaged and background/fluorescence corrected Raman response, δ is the Raman shift, δ_n is the position of n Raman band, $\Delta = 25$ cm^{-1} in the present case. The averaged for the spectral range δ_{min} (1200 cm^{-1})–δ_{max} (1700 cm^{-1}) enhancement factors for Raman scattering G_S^* and luminescence emission G_F^* have been calculated using

$$G_F^* = \int_{\delta_{min}}^{\delta_{max}} F(\delta)\mathrm{d}\delta \quad (2a)$$

$$G_S^* = \int_{\delta_{min}}^{\delta_{max}} I(\delta)\mathrm{d}\delta \quad (2b)$$

where $F(\delta)$ is the intensity of averaged and background corrected total response. The value of G_F^* is slightly overestimated owing to the small input from Raman scattering.

The actual experimental Raman enhancement factor[71,75] G_v, taking into account the size of the beam spot and the size of the enhanced volume under the tip, was estimated using the following assumptions. The volume probed by μ-Raman is estimated as the volume of cell envelope (for the reason for this, see the Results and Discussion sections) because the laser beam covers the cell as a whole. The volume probed by μ-TERS is estimated as the enhanced area under the tip (circle with radius R) multiplied by the thickness of cell envelope (above 100 nm). In the last case we neglect the decrease in intensity of the evanescent field with distance from the surface, so the actual volume will be overestimated and the final G_v value will be the lower estimate. Finally, the enhancement factor G_v is calculated using

$$G_V = G_S \frac{(4\pi Z^2)L}{(\pi R^2)L} = G_S\, 4\left(\frac{Z}{R}\right)^2 \approx G_S\, 400 \quad (3)$$

where Z and R are the radii of the cells (greater than 5 μm in diameter) and the tip apex (greater than 500 nm in diameter) respectively. L is the cell envelope thickness (greater than 100 nm).

Experimental procedure

For the preparation of samples the growing cells were transferred onto a glass slide (Fig. 3, '1'). To determine the homogeneity of cell colonies the optical images in different regions of

the sample were analyzed (Fig. 3, '2') and the optimal location within a sample was imaged by AFM (Fig. 3, '3'). AFM imaging offers a clearer view of cell structure and allows the separation of the living cells at the stationary phase from the budding yeast (Fig. 3, 'f', real typical image) and dead cells (Fig. 3, 'e', real typical image); during this stationary phases the cell monitors its environment and its own size without nucleus replication.[76] Then the selected cells were analyzed by μ-Raman (Fig. 3, '5' and '6') followed by μ-TERS measurements (Fig. 3, '6'). Finally, AFM imaging was used to prove that the cells were not disturbed during the analysis and maintained their integrity (Fig. 3, '7').

Results

AFM imaging of wild-type and genetically modified yeast cells

The optical images of the cells transferred from the agar culture media on the glass substrate indicate the similar interfacial structure of yeast colonies for both wild-type and transformed yeast cells (*e.g.* Fig. 3, 'a' as typical image). AFM imaging verifies this conclusion and resolves the detailed structural features on the cell surface providing better visualization of the 3D structures of the cells.

Fig. 4 shows typical AFM images taken from the colony containing several yeast cells (mainly in monolayer) on the glass. The growth of yeast cells is observed as compact colonies on the substrate; the living cells on the surface held together by an extensive and dense structure. In line with observations from optical microscopy there is no essential difference in the cell growth at the colony's level; the size of the single cells, their distribution inside the colony *etc.* are similar for both wild-type and genetically modified yeast cells.

The imaging on yeast cells has advanced to higher resolution due to the existence of more rigid surface layers (cell wall).[77,78] Therefore, high-resolution AFM imaging of the cells of living yeast is possible and is presented in Fig. 5 for both cell types. In contrast to the surface of wild-type cells, some interfacial structures on the cell wall of modified cells have been observed. The average size of the typical interfacial structures (estimated by statistical analysis using two-dimensional power spectral density function) is greater than 40–60 nm in diameter and 3–5 nm in height – it is greater than the size of a single GDH protein (approximately 38–55 kDa (ref. 79) and 4–6 nm in diameter). However, it is well known that the active form of GDH protein appears to be a homomeric dimer (with 104 kDa (ref. 80)) or tetramer (with weights between 200 and 280 kDa (ref. 81)). In this case the natural active units of GDH can reach 20–30 nm in diameter; additional clustering of stable GDH multimer is also possible. The topography features on AFM images (Fig. 5, top inserts) correlate well with the "dark areas" in the phase diagrams; the last one clearly visualizes the round shape of surface substructures. The dark regions on the phase diagrams have a similar size to the elevated segments of the surface and their arrangement correlates with the arrangement of the faces of the individual clusters. This suggests that the existence of "dark areas" in the region of the peaks may be related not so much to real variations of the surface composition as to the features of the surface profile.[82]

So, we can assume that the outer cell wall is constructed from the same material for both cell types and the observed "mountains" are the result of the formation of subsurface clusters *etc.* To verify this observation, force spectroscopy measurements have been performed which indicate the mechanical properties[83,84] of the cells. The similar AFM force–displacement curves for both wild-type and genetically modified yeast cells (data shown in the ESI†) indicate that cell walls have similar local composition in both wild-type and genetically modified cells. The stretching of the cell wall in the last case compensates for the increased osmotic pressure induced by the synthesis of additional GDH proteins and is clearly visualized by profiling the cell surface presented in Fig. 5. The presence of membrane folds in the micro-scale, easily observed in case of wild-type cells, gave way to a smooth surface with local structure specific to the nano-scale with regards to genetically modified yeast cells.

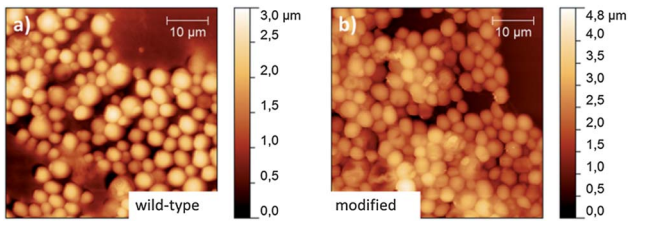

Fig. 4 AFM image of living yeast cells: (a) colony of wild-type cells and (b) colony of genetically modified cells.

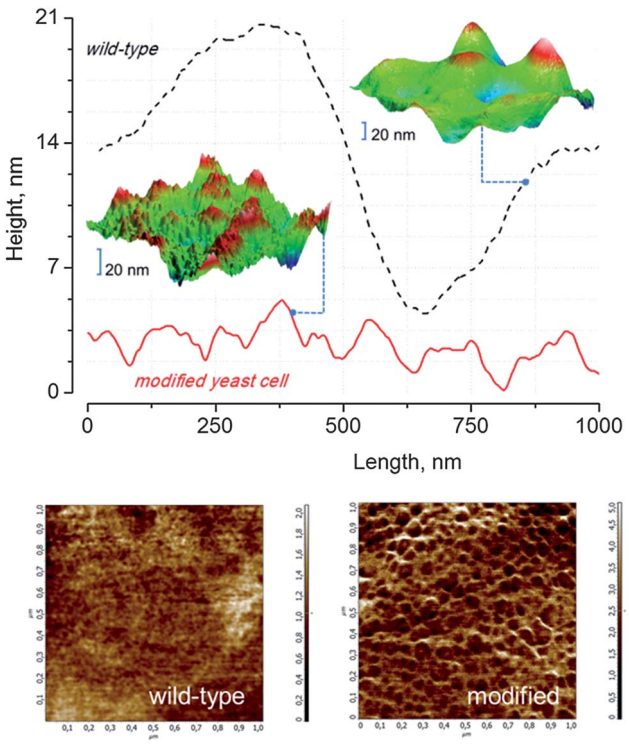

Fig. 5 The typical profiles of topography (top) and full phase images (bottom) of the surface of cellular membrane of wild-type and genetically modified yeast cells. Insert indicates high-resolution topographical (2 × 2 μm) imaging (2D data in the ESI†).

Single-cell Raman spectroscopy: measurement conditions

A suitable approach to analyze or fingerprint the chemical composition of the cell is the use of vibrational spectroscopy. The spatial resolution of confocal μ-Raman spectroscopy in the low micrometer scale and its ability to probe samples under *in vivo* conditions (both water and air are transparent to visible light enabling molecular imaging analysis) allow to monitor the chemical composition of the living single cell without the need for chemical fixatives, markers or stains.[85,86] One widely used approach is to employ optical tweezers, which provide an excellent tool to study non-adherent cells by immobilizing them in solution.[87] The alternative approaches are based on dropping the cells on a modified glass slide, with or without further sealing with a cover-glass for mechanical fixation of the cell wall.[88] The usage of the procedures mentioned above was based on the dilution of the cell culture followed by centrifugation and washing; in our case one was unsuccessful due to the damage of genetically modified cells during these procedures. The attempts to grow the cells directly on quartz slides using standard techniques were also unsuccessful. Finally we used direct transfer of the growing cells from the multi-layered colonies in the Petri dish without any additional fixation procedures before the Raman measurements. However, as mentioned in ref. 89, no Raman scattering peaks of a non-fixed yeast cell deposited on a glass substrate can be detected by a focused beam because of the strong fluorescence interference from the cell and the high "noise" level. The same situation has been observed in our experiments for the case of a focused laser beam. Moreover, increasing the acquisition time (up to 120 s) had no essential effect on the noise level. This effect was more pronounced for wild-type cells with a highly corrugated membrane in respect to more smooth transferred counterparts and in contrast to the spectrum for a single GDH protein. We believe that in the present case the membrane fluctuations are the principal sources of noise arising at the focal plane of the objective within the highest density of the optical field. To decrease this effect by spatial averages within the cell membrane, the size of the laser beam has been increased to a diameter similar to the cell size.

The cell-to-cell spectral variation is low. We attribute the relatively low variations in our study to several factors. First of all, the sampling procedure based on AFM imaging results in selection of the cells, which appear to be very similar morphologically; they were round shaped and were similar in size. Secondly, we used the partly unfocused laser beam to cover the entire cell; therefore, it is likely that intracellular organelles in the different areas within the cell are equiprobably probed. Furthermore, this study examined the live (non-fixed) cells using low-energy (632.8 nm) and low-intensity testing light (above 1 mW per area of 5 μm diameter in the sample plane).

Single-cell Raman spectroscopy: spectra analysis

Fig. 6 shows original as well as averaged and the baseline/fluorescence corrected μ-Raman and μ-TERS spectra of the low-wave region numbered from 1200 to 1700 cm^{-1} for the modified yeast cells in inverted configuration; for clarity the spectra have been spaced on the intensity axis in the same scale.

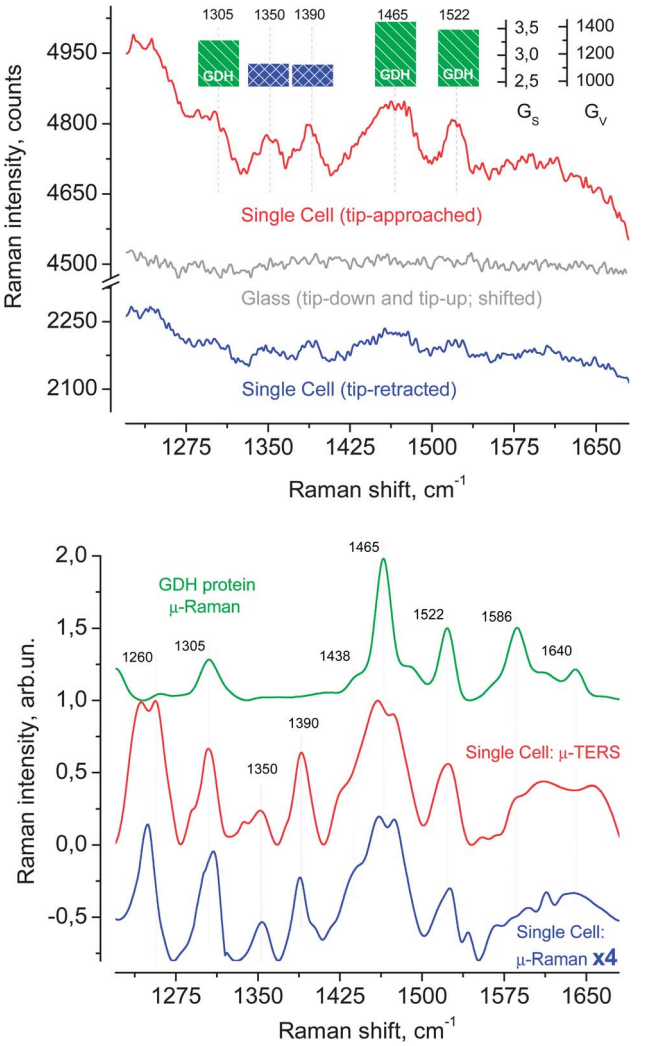

Fig. 6 Top: averaged for 10 raw records original μ-Raman and μ-TERS spectra of genetically modified yeast cells (632.8 nm, 1 mW in the sample plane, acquisition time 30 s), glass substrate (632.8 nm, 1 mW *ibid*., acquisition time 30 s, shifted up for 3700 counts) Bottom: corrected for luminescence background and smoothed spectra from the top as well as the spectra of single GDH protein (532 nm, 1 mW *ibid*., acquisition time 120 s); μ-Raman and μ-TERS sequentially recorded for the same single cell.

The Raman spectra that we obtained from genetically modified cells are similar to the spectra of most living cells,[90] in particular they correlate well with other Raman spectral data obtained from yeast cells.[91] The spectra of modified cells share many typical bands that are indicative of yeast cells, *e.g.* 1664, 1602, 1450, 1305 cm^{-1} *etc.* (Fig. 6). The assignment of individual peaks has been made on the basis of assignments by others and can be found in ref. 92. It is important to note that although some specific assignment can be made, many of the bands are in spectral regions characterized by significant overlap between protein, lipids and polysaccharide peaks. As such, well-defined comparative analysis of the Raman spectra specific for modified and non-modified yeast cells becomes more complex and ambiguous in the present case. Instead of this we analyze the correlation of the single GDH protein spectrum with both μ-Raman (cell averaged) and μ-TERS (enhanced near the outer

cell wall surface) with the aim to answer the questions: Can the single GDH protein spectrum be a part of μ-Raman or/and μ-TERS spectra?

Both spectra, μ-Raman and μ-TERS, were measured consecutively on the same cell. Despite the approximately four-fold increase in the intensity of the bands in the case of μ-TERS, the position and the mutual intensity of the bands remained almost unchanged: most features of the μ-Raman spectra are easily identified in μ-TERS if compared with each other. Two factors may be accountable for that. First of all, for the μ-Raman when the scattered radiation is collected from the entire volume of the cell, the primary contribution is from the cell envelope since the concentration of different components in the cell volume is low whereas homogeneous Rayleigh scattering is higher. From the other side, μ-TERS as well enhances the Raman signal over a wide area of space, covering the membrane completely over its thickness. So, the differences between μ-Raman and μ-TERS are mainly quantitative rather than qualitative.

The yeast cell envelope is made of helical glucans and oligomannans, proteins, lipids, and some chitin[93] and comprises ~30% of the dry weight of the cell. So, it is reasonable to expect that Raman spectra will be a combination of spectra originating from the main fractions: β-1,3-glucan (50% of cell wall) and mannoproteins (40%), whereas the input from other fractions will be low. Indeed, many peaks are well correlated with glucan (*e.g.* 1455, 1360, 1265 cm^{-1})[94] and mannoproteins (1558, 1473, 1428, 1339 cm^{-1} *etc.*).[95] However, the best correspondence can be achieved if we take into account the bands identified in the spectra of GDH protein (Fig. 6); all bands specific to GDH protein (1664, 1640, 1611, 1586, 1568, 1522, 1487, 1465, 1438, 1409, 1371, 1353, 1305, 1260 cm^{-1}) are present in the Raman spectra of genetically modified cells.

Whereas the possible contribution of GDH protein to the full set of cell proteins is relatively low (less than 1% in line with biochemical analysis), the direct identification of the GDH specific fingerprint from the complex response Raman spectra is impossible owing to the similarity of protein spectra. However, at least it is possible to conclude that all GDH specific bands are present in the Raman spectra of the cells.

Single-cell Raman spectroscopy: field enhancement

First of all it is reasonable to note that the observed enhancement of both fluorescence and Raman signals cannot be explained by an additional reflection from the tip approaching the surface. The reasons for that are the conical form of the tip, its small size with respect to the cell and laser beam and the similar signal at a glass surface for both tip-down and tip-up configurations. The difference in amplification levels of luminescence and Raman signals as well confirm this conclusion.

In addition to the enhancement of Raman scattering, the excitation of SPP at the gold tip resulted in the local enhancement of the luminescence signal (originating mainly from porphyrin containing membrane proteins in yeast cells[96]) as well. Comparison of the luminescence emission for a single cell with and without the tip above it revealed that the enhancement factor for luminescence emission is greater than 2.8 for the 1200–1700 cm^{-1} spectral range. The difference between Raman scattering and luminescence emission enhancements can be explained by the difference in the "actual" volumes of signals generating space. For tip–sample distances greater than 10 nm the luminescence signal increases, whereas below this threshold the metal surface quenched the luminescence signal owing to the increase in the rates of non-radiative processes.[97] As such, effective luminescence volume will be less for the space extending to the quenching threshold. In the case of thick samples (greater than the penetration depth of the evanescent wave) this effect may be insignificant. However for thin structures the tip–sample distance must be optimized using maximum luminescence emission as a criterion if a quantitative comparison of Raman and luminescence specific enhancement factors is intended to be determined.

For the case of yeast the thickness of the cell envelope is greater than 100 nm and the difference in effective Raman and luminescence volumes may likely be neglected. In this case the difference between Raman scattering and luminescence emission enhancements is probably related to the difference in enhancement mechanism specific for those processes. Indeed, the mechanism related to the increasing of the cross-section is negligible for the luminescence emission owing to the huge difference in the typical cross-sections exploited by Raman (above 10^{-30} cm^2) and luminescence (above 10^{-16} cm^2) based technologies. This suggestion allows us to estimate the input of the additional mechanism in the total enhancement factor of Raman scattering under μ-TERS conditions. Taking into account that the luminescence enhancement factor G_F^* (related to the amplification of incident light), is above 2.8, and the Raman G_S^*, is above 3.3, the relative input of the addition mechanism in the enhancement factor of Raman scattering is greater than 15%. This value is an upper estimate taking into account the possible bleaching volume effect mentioned above. We suggest that this additional mechanism can be related to the gradient-field Raman[13,14] effect, because one arises from the abnormally large electric field gradient near a metal surface. Under μ-TERS conditions, the evanescent wave itself generates a huge field gradient.[98,99] Moreover, the interaction of a highly compressed optical field of the evanescent wave with the molecular components of a spatially non-uniform cell wall, may give rise to a localized field gradient, which decays on a length scale comparable to that of the induced oscillation.[13,14] It is reasonable to note that in complex organic molecules with a highly-conjugated system and delocalized π-electrons (*e.g.* porphyrins, *etc.*) the molecular vibration may involve numerous atoms of macrocyclic rings and, naturally, occupy a relatively extensive area of space. As the result, the conditions specific for gradient-field Raman may be fulfilled.

Under μ-TERS conditions, the actual experimental Raman enhancement factor G_v, taking into account the size of the beam spot and the size of the enhanced volume under the tip, is greater than 1.3×10^3 (Fig. 6). This enhancement of the Raman signal arises from the multiplication of the enhancement factors due to the compression and confinement of optical energy in the form of the evanescent wave, possible focusing as well as from gradient-field Raman effect. The main enhancing mechanism under μ-TERS conditions is related to the effects of

the optical field compression and confinement near the tip surface owing to SPP generation, with usual field intensity increasing by 10^2–10^3 for the flat surface. Additional amplification can result from partial focusing by the plasmonic tapered waveguide, but in line with theoretical calculations for tips with the radius of curvature more than 50 nm at the apex, the electric field enhancement owing to focussing is less than ten.[100] And, finally, last but not least is the gradient field enhancement based on a strong electric field gradient that shifts the potential energy of the atoms as they move during the vibration.[13,14] This scattering term is dependent on the field gradient and the polarizability tensor, which is responsible for the scattering of visible or near-infrared light.[10,101]

Detailed analysis of the enhancement factors for the various Raman bands in the spectrum of cells shows that the increased amplification (above 20%) is specific for the bands that have contribution from the GDH protein (see the insert in Fig. 6). This difference suggests that the GDH protein is within the area occupied by the evanescent wave and its spatial position differs from the distribution inherent to intrinsic proteins within the cell wall. Indeed, so far as the intensity of the evanescence wave decays exponentially with distance to the interface, the enhancement factor as well will be a function of the distance: if the protein is located near the tip the enhancement factor will be higher, if far away from the tip, the enhancement factor will tend to zero. Thus, a large value for the enhancement factor for the GDH containing bands suggests that the center of mass of the GDH protein distribution is closer to the outer surface of the cell than most natural complexes of the membrane. Given the fact that the predominantly intrinsic protein complexes are located near the inside cell wall (except manno-proteins, uniformly distributed in the volume of the cell wall), the Raman study confirms the results of AFM imaging concerning the preferential location of the GDH proteins within the cell wall.

Discussion

The yeast outer envelope comprises the yeast cell wall (greater than 100 nm), the periplasmic space (3–5 nm) and the plasma membrane (7–10 nm). In *S. cerevisiae*, the cell wall comprises up to 30% of the dry weight of the cell and up to 50% of the volume based on calculations from electron micrographs.[102,103] The cell wall is a highly adaptable organelle; the plasma membrane and cell wall act together to regulate cell volume and therefore the size when appropriate. The yeast cell wall demonstrates the combination of considerable mechanical strength and high elasticity allowing the wall to redistribute physical stress, which offers efficient protection against mechanical damage, in particular, owing to internal pressure. In addition to the stabilization of internal osmotic conditions, the function of protective coat and maintenance of cell shape is also performed—the cell wall is a scaffold for protein. The combination of stress-bearing polysaccharides with glycoprotein (mannoproteins) limits the permeability of the cell wall for outsider macromolecules; conceivably, they may also limit the escape of soluble intracellular components into the medium. The limited

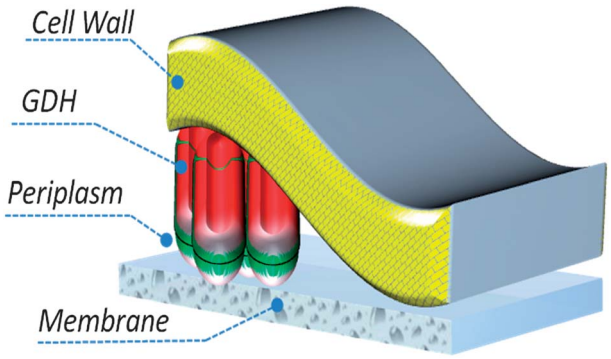

Fig. 7 Schematic diagram of core reactions illustrating the accumulation of the GDH protein by the yeast cell envelope.

permeability of the external protein layer may also allow the creation of a microenvironment in the inner region of the wall adjacent to the plasma membrane.[104] This concept is well correlated with the natural arrangement of GDH proteins within the periplasm of prokaryotic cells.[105]

The short overview of the cell wall construction in *S. cerevisiae* allows the proposal of the clear view of the process occurring as the result of genetic modifications. In the present case the cell wall acts as a passive molecular sieve and retains GDH molecules inside the cell envelope (Fig. 7).

The synthesized GDH protein, in line with analysis of hydrophobicity profiles, shows two potential trans-membrane motives (2–26 aa and 373–392 aa) and thus integrates or crosses the membrane and finally accumulates inside the periplasmic space with possible partial penetration into the polysaccharide cell wall. Owing to strong over-expression, the single protein aggregates (in dimer, tetramer or more) form multimolecular domains inside the cell envelope. So, the yeast periplasm accumulates 'secreted' GDH proteins that are unable to permeate the cell wall, but remain associated with the cell membrane (Fig. 7). These explanations are consistent with the results from the AFM studies—we found that the surface of transformed cells at the nano-scale was rougher (protein domains under the cell wall), whereas in micro-scale, it was essentially smoother (higher osmotic pressure due to GDH protein over-expression) than that of untreated controls. The chemical analysis specific to the cell wall of yeast using μ-TERS also reveals the presence of the GDH protein inside the cell envelope—all GDH-specific Raman bands were identified. Our biochemical investigation of the enzyme activity of genetically modified yeast cells also links maximal GDH activity to solubilised membrane proteins.[106] Glucose dehydrogenase activity was measured in separated cytoplasmic and membrane fractions of modified yeast cells, as well as in the extracellular medium, concentrated up to 100 times. It was found that maximal GDH activity is in the solubilised membrane protein fraction (~40 U mL^{-1}) compared to that localized in cytoplasm (29 U mL^{-1}) or secreted form (trace amounts).

Conclusions

In the present work we have compared the wild-type and genetically modified yeast cells using the changes in the cell

wall topography as criteria. The combination of Atomic Force Microscopy with the μ-Raman and μ-TERS spectroscopy for studying the structure and chemical composition of biological objects allowed us to determine that genetic modification leads to the stretching and smoothing of the cell envelope enriched by GDH proteins assembled together in multiprotein clusters. This result has been verified by conventional biochemical studies.

The reason for such a strong accumulation of the protein in the cell envelope is the peculiarities of the gene construct used in this case. The presence of *Kluyveromyces lactis* toxin signal sequence in the genetic design of GDH assumes the secretion of the synthesized protein into the extracellular medium. However, as shown in our study, despite the intense protein synthesis in the cell (the intensity of luminescence is more than 1.5 times higher for modified with respect to the non-modified yeast cells), its output to the extracellular environment does not occur. Instead, the protein accumulates in large quantities in the cell envelope without cell death. Such clustering may cause "jamming" of the protein near the cell wall and prevent its release into the extracellular medium. Thus, the presence of trans-membrane fragments, together with a tendency to cluster, causes the accumulation of the protein within the periplasmic space. These explanations are consistent with both the results from the AFM and Raman studies confirmed by the biochemical data.

Finally, we demonstrate that the combination of scanning probe microscopy with μ-tip enhanced optical readout provides a 'window' into the cell's life. Subwavelength light confinement in the form of an evanescent wave supported by propagating surface plasmon polaritons open the way for on-line monitoring of subsurface processes near or within the cell envelope, inaccessible by other methods. In some sense the μ-TERS technique is similar to classical biosensor systems based on the propagating surface plasmon resonance phenomenon[18] but with sensitive elements a few micrometers in size that can be targeted to the area of interest; in addition to the detection of total characteristics of the volume under the tip, the use of Raman scattering as an informative signal opens the way for fingerprinting, identification and possible monitoring of specific components. We hope that further development of μ-TERS technology makes it possible not only to track the biological transformations at the subcellular level, but also to elucidate morphological and biochemical changes of cells *in vivo* using label-free subsurface imaging of cell membrane components.

Acknowledgements

The authors thank Prof. Juozas Kulys for his interest and support of this work, Dr T. Jokantaite (Nature Research Center, Vilnius) for the *S. cerevisiae* strain 21PMR (MATα*leu2ura3-52*), Andrius Stogrin (Kaunas University of Technology) for the preparation of gold tips and European Community Mobility Programme EMA2 (B.S.). This research was funded by the European Social Fund under the Global Grant measure. The authors would also like to express their sincere thanks to all anonymous reviewers for their critical comments and useful suggestions that improved the final version of the article.

Notes and references

1 D. Klenerman, Y. E. Korchev and S. J. Davis, *Curr. Opin. Chem. Biol.*, 2011, **15**, 696–703.
2 H. J. van Manen, Y. M. Kraan, D. Roos and C. Otto, *Proc. Natl. Acad. Sci. U. S. A.*, 2005, **102**, 10159–10164.
3 Y. S. Huang, T. Karashima, M. Yamamoto and H. Hamaguchi, *Biochemistry*, 2005, **44**, 10009–10019.
4 M. Harz, P. Roesch and J. Popp, *Cytometry, Part A*, 2009, **75**, 104–113.
5 Q. Tu and C. Chang, *Nanomed.: Nanotechnol., Biol. Med.*, 2012, **8**, 545–558.
6 A. Ulcinas, G. Valdre, V. Snitka, M. Miles, P. M. Claesson and M. Antognozzi, *Langmuir*, 2011, **27**, 10351–10355.
7 R. M. Stockle, Y. F. Suh, V. Deckert and R. Zenobi, *Chem. Phys. Lett.*, 2000, **318**, 131–136.
8 B. Pettinger, B. Ren, G. Picardi, R. Schuster and G. Ertl, *Phys. Rev. Lett.*, 2004, **92**, 096101–096105.
9 P. Verma, T. Ichimura, T. Yano, Y. Saito and S. Kawata, *Laser Photonics Rev.*, 2010, **4**, 548–561.
10 D. Mehtani, N. Lee, R. D. Hartschuh, A. Kisliuk, M. D. Foster, A. P. Sokolov and J. F. Maguire, *J. Raman Spectrosc.*, 2005, **36**, 1068–1075.
11 K. Kneipp, *Phys. Today*, 2007, **60**, 40–46.
12 D. Cialla, A. März, R. Böhme, F. Theil, K. Weber, M. Schmitt and J. Popp, *Anal. Bioanal. Chem.*, 2012, **403**, 27–54.
13 E. J. Ayars, H. D. Hallen and C. L. Jahncke, *Phys. Rev. Lett.*, 2000, **85**, 4180–4183.
14 H. D. Hallen, *NanoBiotechnology*, 2007, **3**, 197–202.
15 *Surface-Enhanced Raman Scattering. Physics and Applications. Series: Topics in Applied Physics*, ed. K. Kneipp, M. Moskovits and H. Kneipp, 2006, vol. 103.
16 D. A. Woods and C. D. Bain, *Analyst*, 2012, **137**, 35–48.
17 C. Ciracì, R. T. Hill, J. J. Mock, Y. Urzhumov, A. I. Fernández-Domínguez, S. A. Maier, J. B. Pendry, A. Chilkoti and D. R. Smith, *Science*, 2012, **337**, 1072–1074.
18 B. A. Snopok, *Theor. Exp. Chem.*, 2012, **48**, 283–306.
19 K. A. Willets and R. P. Van Duyne, *Annu. Rev. Phys. Chem.*, 2007, **58**, 267–297.
20 J. N. Anker, W. P. Hall, O. Lyandres, N. C. Shah, J. Zhao and R. P. Van Duyne, *Nat. Mater.*, 2008, **7**, 442–453.
21 M. Asghari-Khiavi, B. R. Wood, P. Hojati-Talemi, A. Downes, D. McNaughton and A. Mechler, *J. Raman Spectrosc.*, 2012, **43**, 173–180.
22 M. I. Stockman, *Phys. Today*, 2011, **64**, 39–44.
23 V. V. Klimov, *Nanoplasmonics*, Fizmatlit, Moscow, 2010.
24 M. I. Stockman, *Nano Lett.*, 2006, **6**, 2604–2608.
25 W. Zhu, I. D. Rukhlenko and M. Premaratne, *IEEE Photonics J.*, 2012, **4**, 741–747.
26 A. Passian, A. Wig, A. L. Lereu, P. G. Evans, F. Meriaudeau, T. Thundat and T. L. Ferrell, *Ultramicroscopy*, 2004, **100**, 429–436.
27 J. A. Schuller, *Nat. Mater.*, 2010, **9**, 193–204.

28 M. I. Stockman, *Phys. Rev. Lett.*, 2004, **93**, 137404.
29 S. Berweger, J. M. Atkin, R. L. Olmon and M. B. Raschke, *J. Phys. Chem. Lett.*, 2012, **3**, 945–952.
30 S. Berweger, J. M. Atkin, R. L. Olmon and M. B. Raschke, *J. Phys. Chem. Lett.*, 2010, **1**, 3427–3432.
31 V. Snitka, R. D. Rodriguez and V. Lendraitis, *Microelectron. Eng.*, 2011, **88**, 2759–2762.
32 H. Dehez, A. April and M. Piché, *Opt. Express*, 2012, **20**, 14891–14905.
33 B. A. Snopok, S. Darekar and E. V. Kashuba, *Analyst*, 2012, **137**, 3767–3772.
34 P. M. Boltovets, O. M. Polischuk, O. G. Kovalenko and B. A. Snopok, *Analyst*, 2013, **138**, 480–486.
35 M. I. Stockman, *Opt. Express*, 2011, **19**, 22029–22106.
36 M. Q. Zhang, R. Wang, X. B. Wu and J. P. Wang, *Sci. China, Ser. G: Phys., Mech. Astron.*, 2012, **55**, 1335–1344.
37 H. M. Barlow and A. L. Cullen, *Proc. Inst. Electr. Eng.*, 1953, **100**, 329–347.
38 K. Hasegawa, J. U. Noeckel and M. Deutsch, *Phys. Rev. A: At., Mol., Opt. Phys.*, 2007, **75**, 063816.
39 D. R. Mason, D. K. Gramotnev and K. S. Kim, *Opt. Express*, 2012, **20**, 12866–12876.
40 S. Lysenko, B. Snopok and V. Sterligov, *Opt. Spectrosc.*, 2010, **108**, 581–590.
41 A. Savchenko, E. Kashuba, V. Kashuba and B. Snopok, *Sens. Lett.*, 2008, **6**, 705–713.
42 A. Downes, D. Salter and A. Elfick, *J. Microsc.*, 2008, **229**, 184–188.
43 A. Hartschuh, E. J. Sánchez, X. S. Xie and L. Novotny, *Phys. Rev. Lett.*, 2003, **90**, 095503–095507.
44 N. Anderson, A. Hartschuh, S. Cronin and L. Novotny, *J. Am. Chem. Soc.*, 2005, **127**, 2533–2537.
45 J. Steidtner and B. Pettinger, *Phys. Rev. Lett.*, 2008, **100**, 236101.
46 T.-A. Yano, P. Verma, Y. Saito, T. Ichimura and S. Kawata, *Nat. Photonics*, 2009, **3**, 473–477.
47 M. B. Raschke and C. Lienau, *Appl. Phys. Lett.*, 2003, **83**, 5089–5091.
48 B. Pettinger, K. F. Domke, D. Zhang, R. Schuster and G. Ertl, *Phys. Rev. B: Condens. Matter Mater. Phys.*, 2007, **76**, 113409–113413.
49 H. Raether, *Surface plasmons on smooth and rough surfaces and on gratings*, Springer-Verlad, Berlin, 1985.
50 B. A. Snopok, K. V. Kostyukevych, O. V. Rengevych, Y. M. Shirshov, E. F. Venger, I. N. Kolesnikova and E. V. Lugovskoi, *Semicond. Phys., Quantum Electron. Optoelectron.*, 1998, **1**, 121–134.
51 G. Y. Fraikin, M. G. Strakhovskaya and A. B. Rubin, *J. Photochem. Photobiol., B*, 1996, **34**, 129–135.
52 J. A. Lippincott-Schwartz, *Annu. Rev. Biochem.*, 2011, **80**, 327–332.
53 A. Castellanos-Gomez, C. R. Arroyo, N. Agraït and G. Rubio-Bollinger, *Microsc. Microanal.*, 2012, **18**, 353–358.
54 R. D. Rodriguez, E. Sheremet, S. Müller, O. D. Gordan, A. Villabona, S. Schulze, M. Hietschold and D. R. T. Zahn, *Rev. Sci. Instrum.*, 2012, **83**, 123708–123716.
55 C. Baldari, J. Murray, G. Ghiara and C. Galeotti, *EMBO J.*, 1987, **6**, 229–234.
56 E. Servienė, S. Pilevičienė and V. Časaitė, *Rom. Biotechnol. Lett.*, 2010, **15**, 5773–5780.
57 J. Sambrook and D. W. Russel, *Molecular cloning: A Laboratory Manual*, Cold Spring Harbor Laboratory Press, New York, 2001.
58 D. M. Woodcock, P. J. Crowther, J. Doherty, S. Jefferson, E. Decruz, M. Noyer-Weidner, S. S. Smith, M. Z. Michael and M. W. Graham, *Nucleic Acids Res.*, 1989, **17**, 3469–3478.
59 F. M. Ausubel, *Short protocols in Molecular Biology*, John Wiley & Sons, NewYork, 4th edn, 1999.
60 H. Birnboim and J. Doly, *Nucleic Acids Res.*, 1979, **7**, 1513–1523.
61 R. Gietz and R. Woods, *Methods Enzymol.*, 2002, **350**, 87–96.
62 V. A. Kalyuzhin, *J. Gen. Biol.*, 2011, **72**, 140–149.
63 F. Sherman, *Yeast genetics, in The Encyclopedia of Molecular Biology and Molecular Medicine*, ed. R. A. Meyers, VCH Publisher, Weinheim, 1997, vol. 6, p. 302.
64 W. Zhang, B. S. Yeo, T. Schmid and R. Zenobi, *J. Phys. Chem. C*, 2007, **111**, 1733–1738.
65 B. Ren, G. Picardi and B. Pettinger, *Rev. Sci. Instrum.*, 2004, **75**, 837–841.
66 X. Wang, Z. Liu, M.-D. Zhuang, H.-M. Zhang, X. Wang, Z.-X. Xie, D.-Y. Wu, B. Ren and Z.-Q. Tian, *Appl. Phys. Lett.*, 2007, **91**, 101105.
67 C. Williams and D. J. Roy, *J. Vac. Sci. Technol., B: Microelectron. Nanometer Struct.–Process., Meas., Phenom.*, 2008, **26**, 1761–1764.
68 A. Savchenko, E. Kashuba, V. Kashuba and B. Snopok, *Anal. Chem.*, 2007, **79**, 1349–1355.
69 A. Bek, F. De Angelis, G. Das, E. Di Fabrizio and M. Lazzarino, *Micron*, 2011, **42**, 313–317.
70 D. K. Gramotnev and S. I. Bozhevolnyi, *Nat. Photonics*, 2010, **4**, 83–91.
71 M. Lucasa and E. Riedo, *Rev. Sci. Instrum.*, 2012, **83**, 061101.
72 S. S. Kharintsev, G. G. Hoffmann, P. S. Dorozhkin, G. de With and J. Loos, *Nanotechnology*, 2007, **18**, 315502–315511.
73 L. A. Reisner, A. Cao and A. K. Pandya, *Chemom. Intell. Lab. Syst.*, 2011, **105**, 83–90.
74 A. Cao, A. K. Pandya, G. K. Serhatkulu, R. E. Weber, H. Dai, J. S. Thakur, V. M. Naik, R. Naik, G. W. Auner, R. Rabah and D. C. Freeman, *J. Raman Spectrosc.*, 2007, **38**, 1199–1205.
75 J. Stadler, T. Schmid and R. Zenobi, *Nanoscale*, 2012, **4**, 1856–1870.
76 G. P. Singh, G. Volpe, C. M. Creely, H. Grötsch, I. M. Geli and D. Petrov, *J. Raman Spectrosc.*, 2006, **37**, 858–864.
77 D. J. Müller and Y. F. Dufrêne, *Trends Cell Biol.*, 2011, **21**, 461–469.
78 H. Feldman, *Yeast: Molecular and Cell Biology*, Wiley-VCH Verlag, Weinheim, 2010.
79 S. Gezici and G. F. Domagk, *J. Biochem.*, 1979, **10**, 427–432.
80 R. A. Rangel-Porras, V. Meza-Carmen, G. Martinez-Cadena, J. C. Torres-Guzmán, G. A. González-Hernández, J. Arnau and J. F. Gutiérrez-Corona, *Mol. Genet. Genomics*, 2005, **274**, 354–363.

81 C. Y. Lee, C. H. Langley and J. Burkhart, *Anal. Biochem.*, 1978, **86**, 697–706.
82 B. Snopok, P. Boltovets and F. Rowell, *Theor. Exp. Chem.*, 2008, **44**, 165–171.
83 B. Strilić, J. Eglinger, M. Krieg, M. Zeeb, J. Axnick, P. Babál, D. J. Müller and E. Lammert, *Curr. Biol.*, 2010, **20**, 2003–2009.
84 H. Schillers, M. Wälte, K. Urbanova and H. Oberleithner, *Biophys. J.*, 2010, **99**, 3639–3646.
85 P. Rosch, M. Harz, M. Schmitt and J. J. Popp, *J. Raman Spectrosc.*, 2005, **36**, 377–379.
86 Y. Naito, A. Toh and H. Hamaguchi, *J. Raman Spectrosc.*, 2005, **36**, 837–839.
87 G. P. Singh, C. M. Creely, G. Volpe, H. Grotsch and D. Petrov, *Anal. Chem.*, 2005, **77**, 2564–2568.
88 Y. S. Huang, T. Karashima, M. Yamamoto and H. Hamaguchi, *J. Raman Spectrosc.*, 2003, **34**, 1–3.
89 J. Chen, B. Shen, G. Qin, X. Hu, L. Qian, Z. Wang, S. Li, Y. Ren and L. Zuo, *J. Phys. Chem. C*, 2012, **116**, 3320–3328.
90 J. Chan, S. Fore, S. Wachsmann-Hogiu and T. Huser, *Laser Photonics Rev.*, 2008, **2**, 325–349.
91 P. Roesch, M. Harz, K. D. Peschke, O. Ronneberger, H. Burkhardt and J. Popp, *Biopolymers*, 2006, **82**, 312–316.
92 A. Sujith, T. Itoh, H. Abe, K. I. Yoshida, M. S. Kiran, V. Biju and V. Ishikawa, *Anal. Bioanal. Chem.*, 2009, **394**, 1803–1809.
93 E. Cabib, D. H. Roh, M. Schmidt, L. B. Crotti and A. Varma, *J. Biol. Chem.*, 2001, **276**, 19679–19682.
94 M. Novak, A. Synytsya, O. Gedeon, P. Slepička, V. Prochazka, A. Synytsya, J. Blahovec, A. Hejlova and J. Copikova, *Carbohydr. Polym.*, 2012, **87**, 2496–2504.
95 J. F. Li, Y. F. Huang, Y. Ding, Z. L. Yang, S. B. Li, X. S. Zhou, F. R. Fan, W. Zhang, Z. Y. Zhou, D. Y. Wu, B. Ren, Z. L. Wang and Z. Q. Tian, *Nature*, 2010, **464**, 392–395.
96 V. N. Karnaukhov, *Luminescent analysis of cells*, Analytical microscopy, Puschino, 2002.
97 E. Dulkeith, A. C. Morteani, T. Niedereichholz, T. A. Klar, J. Feldmann, S. A. Levi, F. C. J. M. van Veggel, D. N. Reinhoudt, M. Moller and D. I. Gittins, *Phys. Rev. Lett.*, 2002, **89**, 203002.
98 M. Gu, J.-B. Haumonte, Y. Micheau, J. W. M. Chon and X. Gan, *Appl. Phys. Lett.*, 2004, **84**, 4236–4238.
99 L. Fedorenko, S. Mamykin, O. Lytvyn, Y. Burlachenko and B. Snopok, *Plasmonics*, 2011, **6**, 363–371.
100 F. De Angelis, G. Das, P. Candeloro, M. Patrini, M. Galli, A. Bek, M. Lazzarino, I. Maksymov, C. Liberale, L. C. Andreani and E. Di Fabrizio, *Nat. Nanotechnol.*, 2010, **5**, 67–72.
101 M. Sun, Y. Fang, Z. Yang and H. Xu, *Phys. Chem. Chem. Phys.*, 2009, **11**, 9412–9419.
102 P. N. Lipke and R. Ovalle, *J. Bacteriol.*, 1998, **180**, 3735–3740.
103 V. Dupres, Y. F. Dufrêne and J. J. Heinisch, *ACS Nano*, 2010, **28**, 5498–5504.
104 F. S. Klis, A. Boorsma and P. W. J. De Groot, *Yeast*, 2006, **23**, 185–202.
105 B. McNeil and L. Harvey, *Nat. Biotechnol.*, 2005, **23**, 186–187.
106 S. Pileviciene, A. Lebionka and E. Serviene, *Proc. Natl. Acad. Sci. Belarus, Chem. Ser.*, 2010, **4**, 209–212.